NJC

ROYAL SOCIETY OF CHEMISTRY

PAPER

View Article Online
View Journal | View Issue

Cite this: *New J. Chem.*, 2021, **45**, 3335

Insight into facet-dependent photocatalytic H_2O_2 production on BiOCl nanosheets

Yating Xu, Hanping Fu, Ling Zhao, Lishan Jian, Qingshuang Liang * and Xiufeng Xiao*

Received 11th November 2020,
Accepted 8th January 2021

DOI: 10.1039/d0nj05506a

rsc.li/njc

Hydrogen peroxide is an important high-energy product widely used in various fields. Highly efficient semiconductor photocatalysts, especially those that can produce H_2O_2 both from water oxidation and O_2 reduction, are eagerly desired. In this work, BiOCl nanosheets with preferentially exposed (001) and (010) facets were synthesized *via* a simple hydrothermal method. The facet-dependent photocatalytic H_2O_2 generation activities of these BiOCl nanosheets were assessed. The hydrogen peroxide evolution rate of BiOCl(001) is about 2-fold higher than that of BiOCl(010), which is assigned to the higher separation efficiency of photogenerated charge carriers. Interestingly, both the EPR study and active species trapping experiments demonstrate that the generation of H_2O_2 on the BiOCl(001) photocatalyst mostly originates from sequential two step single-electron O_2 reduction, while there are two pathways for photocatalytic H_2O_2 production on BiOCl(010), from both oxygen reduction and water oxidation. This work offers a new strategy to pursue highly efficient semiconductor photocatalysts with two pathways for H_2O_2 production from both water oxidation and O_2 reduction.

Introduction

Hydrogen peroxide (H_2O_2) is an important high-energy product widely used in various fields, acting as both an oxidant and reductant in chemical synthesis, environmental cleaning, fuel cells and the medical field.[1–4] At present, many methods have been developed to produce H_2O_2 on a large scale, including anthraquinone oxidation,[5] direct synthesis from H_2 and O_2 and oxidation of alcohols.[6,7] However, these methods cannot be considered ideal approaches because of the high energy demand, and undesirable by-products, and the mixture of H_2 and O_2 may create a potential explosion hazard. Therefore, an efficient, energy-saving and environmentally friendly method to produce H_2O_2 is highly desired. The conversion of solar energy to chemical fuel is a fascinating approach. Recently, researchers have found that H_2O_2 can be produced through semiconductor photocatalytic processes from O_2 and water.[3,8–10] As typical photocatalysts, TiO_2 and modified TiO_2 could function as effective photocatalysts for H_2O_2 generation under UV light.[9,11] Metal-free polymeric semiconductors based on graphitic carbon nitride have been found to generate H_2O_2 by O_2 reduction under visible light.[12,13] Despite the fact that many semiconductor systems have been and are still being explored for H_2O_2 generation, they still suffer from low efficiency. Highly efficient semiconductor photocatalysts, especially those that can produce H_2O_2 from both water oxidation and O_2 reduction, are eagerly needed.

As photocatalytic reactions take place on the surfaces of semiconductors, the surface properties of photocatalysts are crucial in determining the photocatalytic activity. The surface atom arrangement and coordination intrinsically determine the adsorption of reactant molecules and desorption of product molecules, and the surface transfer between the reactant molecules and photoexcited charges. The facet-dependent reactivity of many photocatalysts has been reported.[14–19] TiO_2 with exposed (101) facets has exhibited selective photocatalytic degradation of methylene orange (MO) in a methylene blue (MB) and methyl orange (MO) mixed solution, whereas TiO_2 with exposed (111) and (001) facets exhibits photocatalytic selectivity for MB.[20] Reduction and oxidation cocatalysts could selectively deposit on the (110) and (010) facets of $BiVO_4$, resulting in much higher activity in both photocatalytic and photoelectrocatalytic water oxidation reactions.[21] Facet engineering offers an exciting direction to pursue highly active new generation photocatalysts.

BiOCl,[22–25] which has a layered structure and an indirect-transition band gap to reduce the recombination probability of the excited electron and the hole, has been explored as a promising photocatalyst in various clean energy and environmental technologies, such as water-splitting,[26–28] N_2 fixation[29,30] and waste water treatment.[31–33] Recent studies have revealed that different facets of BiOCl crystals exhibited distinct photocatalytic activities. For instance, Zhang *et al.*[34] found that due to the cooperative effect

---

Fujian Provincial Key Laboratory of Advanced Materials Oriented Chemical Engineering, College of Chemistry and Material Science, Fujian Normal University, Fuzhou, Fujian 350007, China. E-mail: lqs671@163.com, xfxiao@fjnu.edu.cn

between the surface atomic structure and suitable internal electric fields, BiOCl nanosheets with exposed (001) facets exhibited higher activity for direct semiconductor photoexcitation pollutant degradation under UV-light irradiation. Xiong *et al.*[35] reported that the valence band edge of (110) is more negative than that of (001), suggesting that BiOCl nanosheets with exposed (110) facets possess a higher oxidation potential. It is demonstrated that BiOCl(001) presents higher efficiency in charge separation and higher charge carrier density. Yet Liu *et al.*[36] reported that due to the fact that the (010) surface consists of more terminal bismuth atoms and more surface complexes are formed, BiOCl nanosheets exposing (010) facets exhibit higher activity for photodegradation of 2-naphthol. Nevertheless, in previous studies, BiOCl is mainly investigated for photocatalytic degradation of pollutants and research about exploring high H_2O_2 generation on BiOCl nanosheets is rare. A study of the facet-dependent catalytic activity of H_2O_2 generation on BiOCl nanosheets has not yet been carried out.

In this work, BiOCl nanosheets with preferentially exposed (001) and (010) facets were synthesized *via* a simple hydrothermal method. The facet-dependent photocatalytic H_2O_2 generation activities of these BiOCl nanosheets were assessed. The dominant reactive species involved in the facet-dependent photocatalysis were also identified. The reaction mechanisms of H_2O_2 evolution on the BiOCl(001) and BiOCl(010) samples were investigated and it is found that there are two pathways for photocatalytic H_2O_2 production on BiOCl(010) from both oxygen reduction and water oxidation.

Experimental section

Chemicals

Bismuth nitrate pentahydrate ($Bi(NO_3)_3·5H_2O$), potassium chloride (KCl), sodium hydroxide (NaOH), formate acid (98%), ethanol (75%), *P*-benzoquinone (PBQ) and *tert*-butyl alcohol (TBA) were purchased from Aladdin Industrial Corporation. Deionized water was used throughout this study. All chemicals were used as received without further purification.

Preparation of photocatalysts

Synthesis of BiOCl(010) nanosheets. The BiOCl nanosheets were prepared *via* a facile hydrothermal process as reported.[34] Typically, $Bi(NO_3)_3·5H_2O$ (1 mmol) and KCl (1 mmol) were dissolved in distilled water (15 mL) with constant stirring at room temperature. NaOH solution was then dropwise added into the mixed solution, followed by stirring for 30 min, which was to adjust the pH value to about 6.0. Afterwards, the mixture was transferred to a Teflon-lined stainless autoclave and heated at 160 °C for 24 h, and then cooled to room temperature. The precipitates were collected by centrifugation and washed with ethanol and deionized water repeatedly. Finally, the product was dried at 60 °C in air. The obtained powder was denoted as BiOCl(010).

Synthesis of BiOCl(001) nanosheets

The product was obtained by the same method without adding NaOH solution, which was denoted as BiOCl(001).

Characterization

Transmission electron microscopy (TEM) and high-resolution transmission electron microscopy (HRTEM) images of the samples were taken with a JSM-6700F microscope with a 200 kV accelerating voltage. X-ray powder diffraction (XRD) measurements were recorded on a Bruker D8 ADVANCE with Cu-Kα radiation (λ = 0.1518 nm). X-ray photoelectron spectroscopy (XPS) was carried out with a Thermo ESCALab 250 analyzer operating in constant analyzer energy mode. UV-vis diffuse reflectance spectroscopy (DRS) was carried out on a Lambda 750 nm spectrophotometer equipped with an integrating sphere attachment. The electrochemical analysis was carried out on a Zennium Pro electrochemical workstation (Zahner, Germany) with a standard three-electrode cell. Electron paramagnetic resonance (EPR) measurements were carried out on a Bruker A300 spectrometer to capture the intermediate radicals. The active radical species were trapped by adding 5,5-dimethyl-1-pyrroline *N*-oxide (DMPO) as a spin-trapping reagent. Typically, the experiments for superoxide radicals and hydroxyl radicals were conducted in water or chromatographic purity methanol solution and 5% HCOOH solution containing DMPO within a container, respectively. The detection of $O_2^{\bullet-}$ and $^{\bullet}OH$ was in the air and in an anaerobic environment, respectively. Then the solutions were processed in the dark and under light irradiation (300 W xenon lamp) with stirring for 10 min. After the irradiation, the resulting solution was subjected to analysis at room temperature in a sealed capillary tube.

Photocatalytic activity tests

The photocatalytic activity was evaluated by the generation of H_2O_2. The light source was chosen as a 300 W xenon lamp. Typically, 50 mg of catalyst powder was added into 40 mL aqueous solution containing 5% HCOOH solution in a container with an ice-water bath outside. The reaction solution was stirred in the dark for 30 min before photoirradiation. During the photocatalysis process, 2 mL of the suspension was taken from the container every 10 min, and then centrifuged to remove the photocatalysts. The concentration of H_2O_2 was determined by the titanium sulfate spectrophotometric method.[37] Typically, 2 mL of the suspension taken from the glass container was centrifuged to remove the photocatalysts. Then 2 mL of titanium sulfate was added and reacted for the measurement ($H_2O_2 + Ti^{4+} \rightarrow H_2TiO_4$). When the solution became yellow, the absorbance of the reaction product at 400 nm was measured to calculate the concentration of H_2O_2.[38] According to the standard curves of H_2O_2, the amount of H_2O_2 in the solution can be calculated: abs = $0.287C + 0.068$.

Results and discussion

The BiOCl nanosheets with different exposed facets were prepared by a hydrothermal method. Fig. 1a–h display the different morphology and microstructure of the BiOCl(001) and BiOCl(010) nanosheets. As shown in Fig. 1a, the BiOCl(001) nanosheets are composed of a dimetric sheet-shaped morphology and smooth surface with a width of around 0.5–1 μm. Fig. 1b shows that the BiOCl(010) nanosheets exhibit a well-defined truncated square morphology, and the width of the BiOCl(010) sample is about 1–2.5 μm. The TEM images in Fig. 1c and d further confirm the morphology of the as-prepared nanosheets. In Fig. 1g, the corresponding selected-area electron diffraction (SAED) pattern indicated BiOCl(001) nanosheets with a single-crystalline characteristic. The angle labeled in the SAED pattern is 45°, which is in agreement with the theoretical value of the angle between the (110) and (200) planes, matching well with the [001] zone axis diffraction pattern of BiOCl.[34] Fig. 1e shows the HR-TEM image of the BiOCl(001) sample. The interplanar lattice spacing of 0.275 nm is assigned to the (110) atomic plane, indexed to the [001] zone axis diffraction pattern of BiOCl. The SAED pattern and the HR-TEM both confirm that the BiOCl(001) sample preferentially exposes the (001) plane. Similar characterizations of the BiOCl(010) sample were carried out and the preferentially exposed orientation of [010] is identified. Fig. 1f shows clear lattice fringes of 0.194 nm and 0.267 nm, corresponding to the (200) and (102) atomic planes, respectively. The corresponding SAED pattern of the BiOCl(010) sample is shown in Fig. 1h, and the (002) and (102) planes are observed with an interfacial angle of 43.4°, matching well with those of the [010] zone axis of BiOCl.

XRD was employed to further determine the crystallographic phase of the samples. The XRD patterns of BiOCl(001) and BiOCl(010) are shown in Fig. 2. All diffraction peaks of BiOCl could be indexed to the standard JCPDS: 06-0249, and no diffraction peaks of other impurities were observed, indicating high purity of the BiOCl samples. It can be seen that the (001) peak is the most intense one among all of the peaks of the BiOCl(001) sample, indicating that the as-prepared nanosheets are covered with dominant (001) facets. In addition, the intensity proportions of the (002) and (200) peaks are 2.404 and 1.233 for BiOCl(001) and BiOCl(010), respectively.[34] This difference in the intensity ratios reveals the different crystallization orientations of the BiOCl(001) and BiOCl(010) samples, which is consistent with the HR-TEM and SAED results.

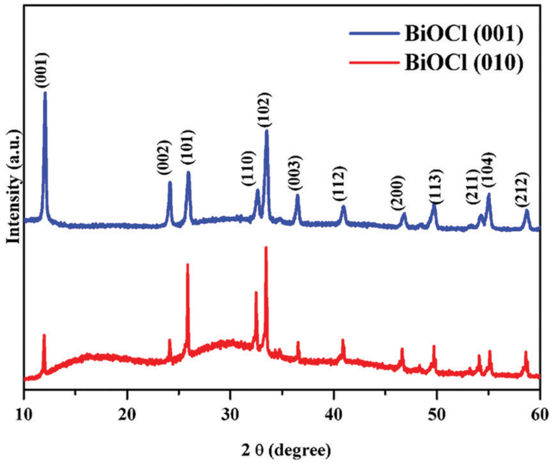

Fig. 2 XRD patterns of the BiOCl(001) and BiOCl(010) samples.

The surface chemical state and composition of the BiOCl(001) and BiOCl(010) samples were analyzed by XPS. Fig. 3a–d display the full XPS survey spectra and the Bi 4f, O 1s and Cl 2p XPS spectra of the BiOCl(001) and BiOCl(010) samples. As shown in the survey spectra (Fig. 3a), bismuth, chlorine, and oxygen species are observed in both samples. For the Bi 4f region, the peaks observed at 164.2 and 158.8 eV are assigned to the spin orbit splitting photoelectrons of Bi ($4f_{5/2}$) and Bi ($4f_{7/2}$) in BiOCl, respectively.[33] Both the Bi $4f_{5/2}$ and $4f_{7/2}$ states can be observed in BiOCl(001) and BiOCl(010), indicating the same chemical state of Bi atoms in these two samples.

Since the BiOCl nanosheets were covered with different dominant facets, their facet-dependent photocatalytic H_2O_2 production performances were tested to be compared. The

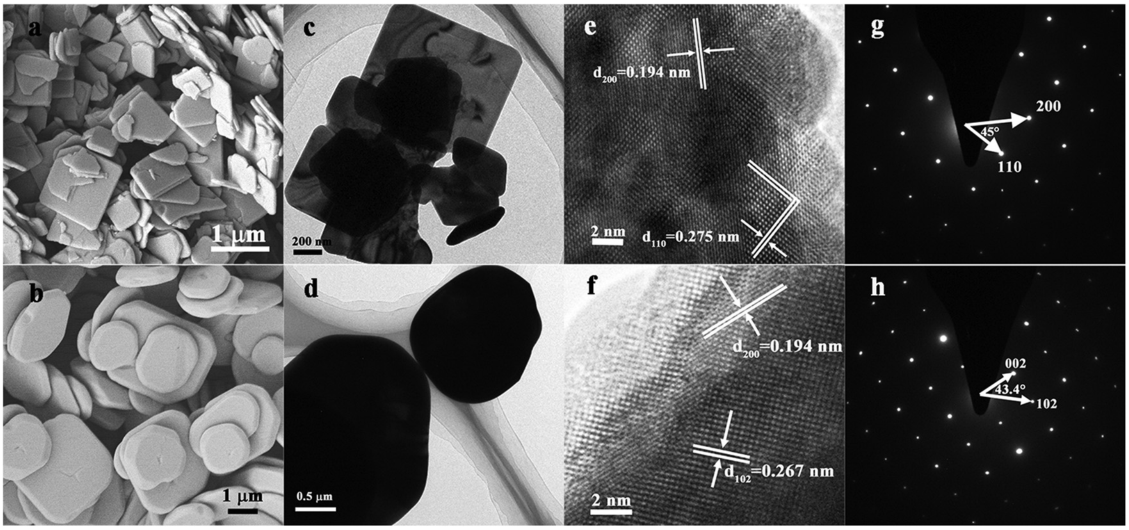

Fig. 1 Electron microscope images of BiOCl(001) and BiOCl(010): (a and b) SEM, (c and d) TEM, (e and f) HR-TEM, and (g and h) SAED.

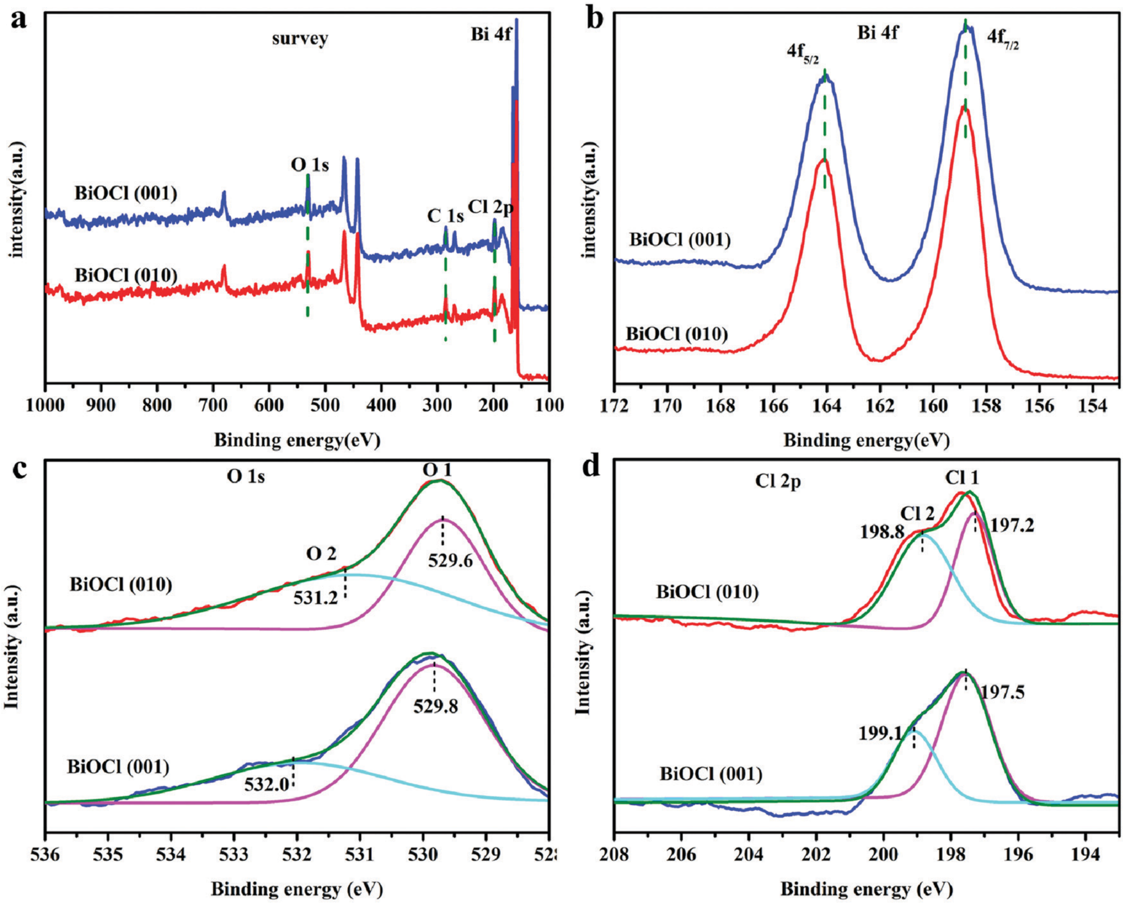

Fig. 3 (a) Full XPS survey spectrum of BiOCl. High-resolution XPS spectra of (b) Bi 4f, (c) O 1S, and (d) Cl 2p for the BiOCl(001) and BiOCl(010) samples.

photocatalytic H_2O_2 production of the BiOCl samples was measured in HCOOH solution. Fig. 4 shows the change of the H_2O_2 concentration with the irradiation time. It can be seen that the concentration of H_2O_2 gradually increases with continued irradiation in both suspensions. After 120 min of irradiation, about 7.1 and 3.3 mmol L^{-1} of H_2O_2 can be rapidly generated over the BiOCl(001) and BiOCl(010) suspensions, respectively. In the same irradiation time, the amount of H_2O_2 generation in the BiOCl(001) suspension is obviously higher than that in the BiOCl(010) suspension. The amount of H_2O_2 generation in the BiOCl(001) suspension is about 2-fold higher than that of the BiOCl(010) sample after 2 h of irradiation. This clearly shows that the as-prepared BiOCl(001) sample exhibits higher photocatalytic H_2O_2 production activity than the BiOCl(010) sample.

Generally, H_2O_2 is produced through oxygen reduction and water oxidation, which occurs through three ways: (1) direct one-electron reduction of O_2 ($O_2 + e^- = O_2^{\bullet-}$) to H_2O_2; (2) multi-electron reduction of O_2 to H_2O_2 ($O_2 + 2H^+ + 2e^- = H_2O_2$) and (3) hole-oxidized-$^{\bullet}$OH ($OH^- + h^+ = {}^{\bullet}OH$) to generate H_2O_2.[37] To uncover the facet-dependent photocatalytic H_2O_2 production over BiOCl nanosheets, the reaction mechanisms of H_2O_2 evolution on the BiOCl(001) and BiOCl(010) samples were investigated, respectively. EPR study with DMPO as the spin-trapping agent was employed to measure the production of active radicals during the photocatalytic process. As shown in Fig. 5, no signals of DMPO-$O_2^{\bullet-}$ and DMPO-$^{\bullet}$OH are observed in the dark. Meanwhile, with light irradiation, characteristic signals of DMPO-$O_2^{\bullet-}$ can be observed on both of the BiOCl(001) and BiOCl(010) samples (Fig. 5a), indicating that both of the BiOCl(001) and BiOCl(010) photocatalysts could generate $O_2^{\bullet-}$ during the photocatalytic process. Therefore, both of the BiOCl(001) and BiOCl(010) photocatalysts could generate H_2O_2

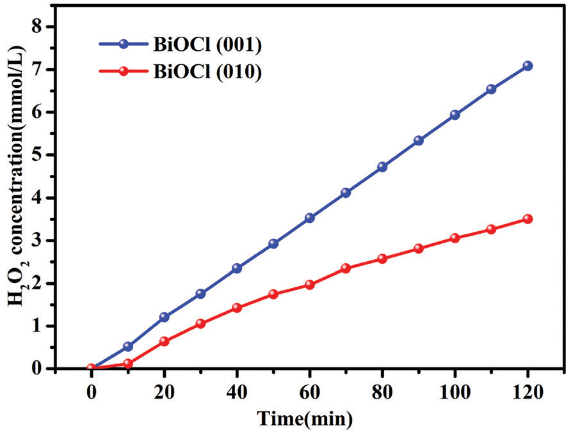

Fig. 4 The concentration of H_2O_2 as the irradiation time-dependent change over the BiOCl(001) and BiOCl(010) samples under light irradiation.

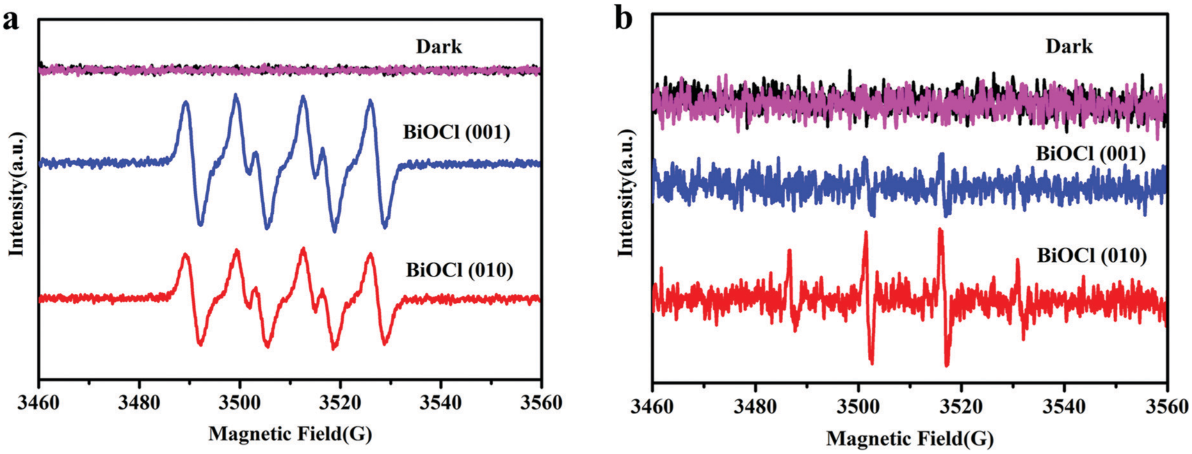

Fig. 5 EPR spectra of active oxygen radicals and hydroxyl radicals generated during BOC(001) and BOC(010) photocatalysis.

through oxygen reduction by a sequential two step single-electron mechanism. Meanwhile, Fig. 5b shows the characteristic peak of DMPO-•OH in the BiOCl(010) samples, indicating that some of the generation of H_2O_2 in BiOCl(010) originated from hole-oxidized-•OH. On the contrary, no obvious DMPO-•OH characteristic peaks are observed in BiOCl(001), indicating that the generation of H_2O_2 on BiOCl(001) is almost all from $O2^{\bullet -}$, the sequential two step single-electron mechanism. Therefore, there are two pathways to produce H_2O_2 on the BiOCl(010) photocatalyst, while the generation of H_2O_2 on BiOCl(001) is mainly by the one-electron reduction of O_2.

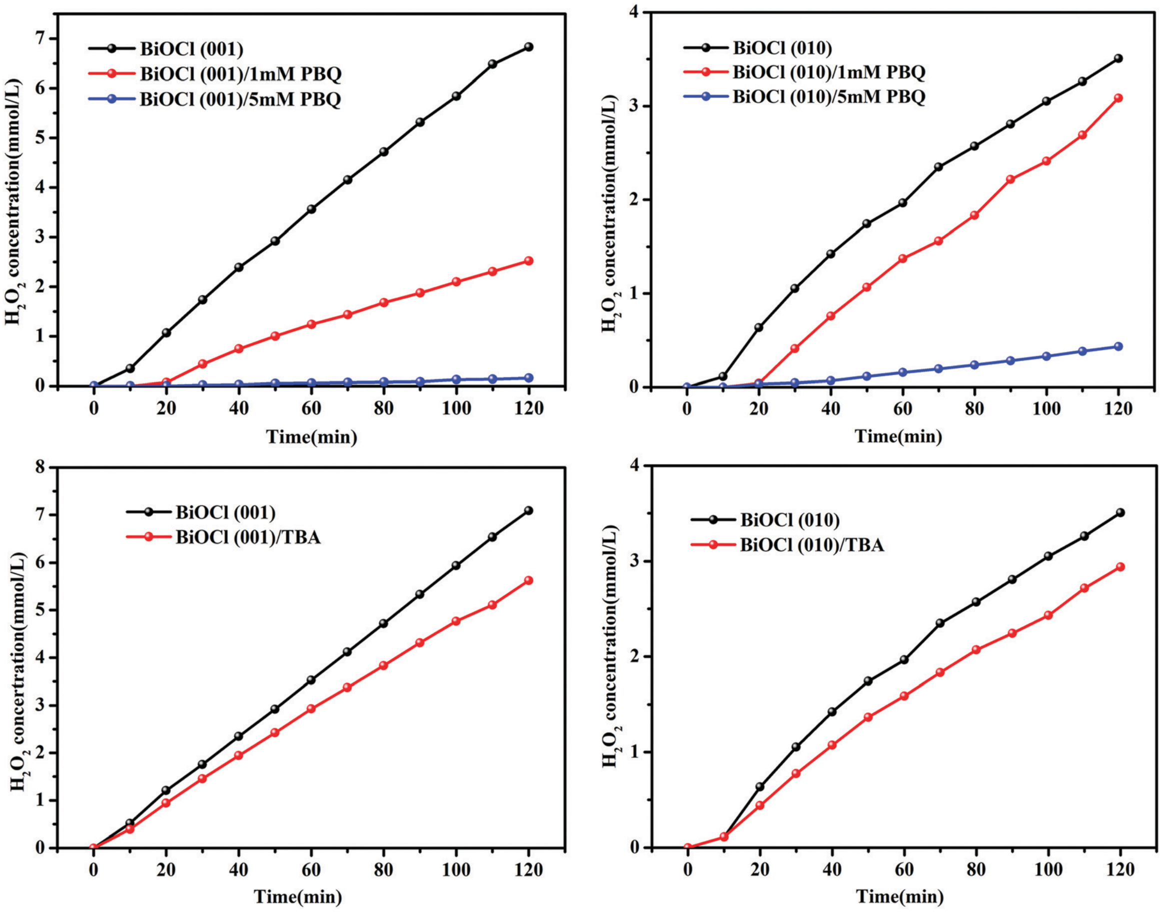

Fig. 6 The influence of scavengers PBQ and TBA on the photocatalytic H_2O_2 production using the BiOCl(001) and BiOCl(010) samples.

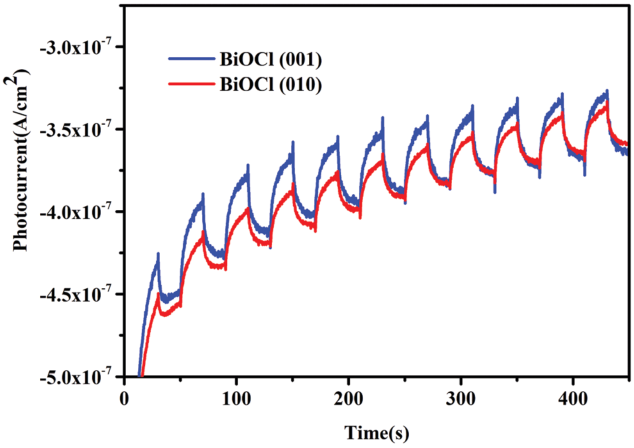

Fig. 7 Transient photocurrent responses of the BiOCl(001) and BiOCl(010) samples.

To further verify the reaction mechanisms of H_2O_2 evolution on the BiOCl(001) and BiOCl(010) samples, a series of active species trapping experiments were conducted. The scavengers *p*-benzoquinone (PBQ) and *tert*-butyl alcohol (TBA) were used to eliminate $O_2^{\bullet-}$ and $^{\bullet}OH$ radicals, respectively. As seen in Fig. 6a and b, the H_2O_2 generation gradually decreases with the PBQ concentration increasing. The generation of H_2O_2 is scarcely observed on the BiOCl(001) photocatalyst when the concentration of PBQ is 5 mM. However, when the concentration of PBQ is 5 mM, the generation of H_2O_2 still exists on the BiOCl(010) photocatalyst. Meanwhile, comparing the BiOCl(001) photocatalyst, the decrease of H_2O_2 generation on the BiOCl(010) sample is more obvious with adding the scavenger TBA (as shown in Fig. 6c and d). These results confirm that the generation of H_2O_2 on the BiOCl(001) photocatalyst mostly originates from sequential two step single-electron O_2 reduction, while the photocatalytic H_2O_2 production on BiOCl(010) can be both from oxygen reduction and water oxidation.

To clarify the facet-dependent photocatalytic H_2O_2 production efficiency of BiOCl nanosheets, an optical absorption performance study and electrochemical analysis were conducted. Fig. 8a shows the UV-vis DRS of the as-prepared BiOCl samples. It can be observed that BiOCl(001) and BiOCl(010) almost have the same light absorption, with similar absorbance

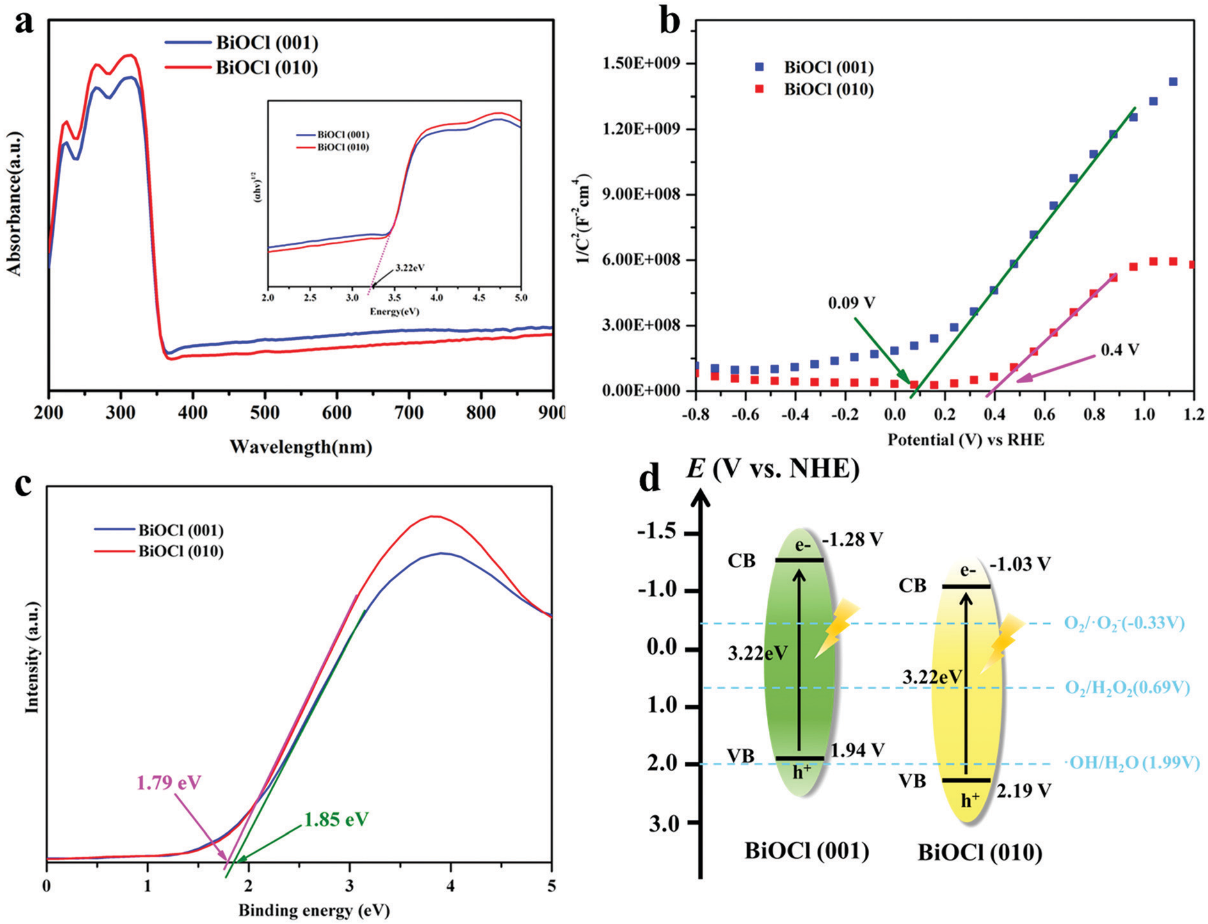

Fig. 8 Band structure between the BiOCl(001) and BiOCl(010) samples. (a) UV-vis absorption spectra and plots of $(\alpha h\nu)^{1/2}$ *versus* energy ($h\nu$) for the BiOCl(001) and BiOCl(010) samples. (b) Mott–Schottky plot of the BiOCl(001) and BiOCl(010) samples. (c) Valence-band XPS spectra of the BiOCl(001) and BiOCl(010) samples. (d) Schematic illustration of the band structure of the BiOCl(001) and BiOCl(010) samples.

edges at about 370 nm. The transient photocurrent response of the as-prepared BiOCl photocatalysts was tested to explore the separation efficiency of photogenerated charge carriers. As shown in Fig. 7, the photocurrent of the BiOCl(001) photocatalyst shows a higher current density than that of the BiOCl(010) photocatalyst. The enhanced photocurrent of the BiOCl(001) photocatalyst indicates the enhanced separation of electrons and holes, then improving the photocatalytic performance. These results demonstrate that the higher photocatalytic H_2O_2 production efficiency of the as-prepared BiOCl(001) sample benefits from the higher separation efficiency of photogenerated charge carriers.

To gain further insight on the facet-dependent photocatalytic H_2O_2 production over BiOCl nanosheets, the corresponding electronic structures of the as-prepared BiOCl samples were investigated. The corresponding band gap energies (E_g) were estimated to be approximately 3.22 eV from DRS spectra (Fig. 8a). Valence-band XPS was used for measuring the valence band position (VB) of the BiOCl(001) and BiOCl(010) nanosheets and Mott–Schottky plots were obtained to estimate the flat-band potentials (Femi level). The flat-band potentials of the BiOCl(001) and BiOCl(010) samples were measured at 0.09 V and 0.4 V *vs.* NHE, respectively (Fig. 8b). As shown in Fig. 8c, the valence band (VB) positions of BiOCl(001) and BiOCl(010) were estimated as 1.94 V and 2.19 V *vs.* NHE, respectively. According to the formula $E_{VB} = E_{CB} + E_g$,[39] the E_{CB} values of BiOCl(001) and BiOCl(010) are calculated to be −1.28 and −1.03 V *vs.* NHE, respectively. Combined with these results, the energy band structures of the BiOCl(001) and BiOCl(010) samples are described in Fig. 8d. As shown in Fig. 8d, since the reduction potential of $O_2/O_2^{\bullet -}$ is −0.33 V, the photogenerated electrons in the CB of both BiOCl(001) and BiOCl(010) have sufficient potential to reduce O_2 to $O_2^{\bullet -}$, which can be further reduced to H_2O_2. Meanwhile, for the photogenerated holes, because the VB potential of BiOCl(010) is more positive than the reduction potential of $OH^-/^{\bullet}OH$, the photogenerated holes in the BiOCl(010) photocatalysts could oxidize OH^- to $^{\bullet}OH$, which might further combine with each other to form H_2O_2. Therefore, the above results demonstrate that the generation of H_2O_2 on the BiOCl(001) photocatalyst mostly originates from sequential two step single-electron O_2 reduction, while the photocatalytic H_2O_2 production on BiOCl(010) is through two pathways from both oxygen reduction and water oxidation. The involved reactions are shown as follows:

$$\text{BiOCl(001)} + \text{visible light} \rightarrow h^+ + e^- \quad (1)$$

$$e^- + O_2 \rightarrow O_2^{\bullet -} \quad (2)$$

$$e^- + O_2^{\bullet -} + 2\,H^+ \rightarrow H_2O_2 \quad (3)$$

$$\text{BiOCl(010)} + \text{visible light} \rightarrow h^+ + e^- \quad (4)$$

$$e^- + O_2 \rightarrow O_2^{\bullet -} \quad (5)$$

$$e^- + O_2^{\bullet -} + 2H^+ \rightarrow H_2O_2 \quad (6)$$

$$h^+ + OH^- \rightarrow {}^{\bullet}OH \quad (7)$$

$$^{\bullet}OH + {}^{\bullet}OH \rightarrow H_2O_2 \quad (8)$$

Conclusions

In summary, BiOCl nanosheets with preferentially exposed (001) and (010) facets were synthesized. The as-prepared BiOCl nanosheets show facet-dependent photocatalytic properties for hydrogen peroxide generation. The hydrogen peroxide evolution rate of BiOCl(001) is about two times higher than that of BiOCl(010), which is assigned to the higher separation efficiency of photogenerated charge carriers. Interestingly, the EPR study, active species trapping experiments and corresponding electronic structure analysis all demonstrate that the generation of H_2O_2 on the BiOCl(001) photocatalyst mostly originates from sequential two step single-electron O_2 reduction, while the photocatalytic H_2O_2 production on BiOCl(010) is through two pathways from both oxygen reduction and water oxidation. This work offers a new strategy to pursue highly efficient semiconductor photocatalysts with two pathways for H_2O_2 production from both water oxidation and O_2 reduction.

Conflicts of interest

There are no conflicts to declare.

Acknowledgements

This work is supported by the National Natural Science Foundation of China (Grant 21805037), Fujian Province Nature Science Foundation (Grants 2016Y0025, 2017J01685, 2019J01021009, 2020J02033) and Fuzhou Science and Technology Project (2017-G-61, 2018-G-90).

Notes and references

1 L. Pi, J. Cai, L. Xiong, J. Cui, H. Hua, D. Tang and X. Mao, *Chem. Eng. J.*, 2019, 123420.
2 G. Zuo, S. Liu, L. Wang, H. Song, P. Zong, W. Hou, B. Li, Z. Guo, X. Meng, Y. Du, T. Wang and V. A. L. Roy, *Catal. Commun.*, 2019, **123**, 69–72.
3 Y. Fu, C. a. Liu, M. Zhang, C. Zhu, H. Li, H. Wang, Y. Song, H. Huang, Y. Liu and Z. Kang, *Adv. Energy Mater.*, 2018, **8**, 1802525.
4 B. O. Burek, D. W. Bahnemann and J. Z. Bloh, *ACS Catal.*, 2018, **9**, 25–37.
5 S. Yang, A. Verdaguer-Casadevall, L. Arnarson, L. Silvioli, V. Čolić, R. Frydendal, J. Rossmeisl, I. Chorkendorff and I. E. L. Stephens, *ACS Catal.*, 2018, **8**, 4064–4081.
6 D. W. Flaherty, *ACS Catal.*, 2018, **8**, 1520–1527.
7 J. Pritchard, L. Kesavan, M. Piccinini, Q. He, R. Tiruvalam, N. Dimitratos, J. A. Lopez-Sanchez, A. F. Carley, J. K. Edwards, C. J. Kiely and G. J. Hutchings, *Langmuir*, 2010, **26**, 16568–16577.
8 M. Teranishi, S.-i. Naya and H. Tada, *J. Phys. Chem. C*, 2016, **120**, 1083–1088.
9 G.-h. Moon, W. Kim, A. D. Bokare, N.-e. Sung and W. Choi, *Energy Environ. Sci.*, 2014, **7**, 4023–4028.

10 Y. Shiraishi, T. Takii, T. Hagi, S. Mori, Y. Kofuji, Y. Kitagawa, S. Tanaka, S. Ichikawa and T. Hirai, *Nat. Mater.*, 2019, **18**, 985–993.

11 M. Teranishi, R. Hoshino, S. Naya and H. Tada, *Angew. Chem.*, 2016, **55**, 12773–12777.

12 S. Li, J. A. Willoughby and O. J. Rojas, *ChemSusChem*, 2016, **9**, 2460–2469.

13 S. Samanta, R. Yadav, A. Kumar, A. K. Sinha and R. Srivastava, *Appl. Catal., B*, 2019, **259**, 118054.

14 F. Guo, J.-H. Guo, P. Wang, Y.-S. Kang, Y. Liu, J. Zhao and W.-Y. Sun, *Chem. Sci.*, 2019, **10**, 4834–4838.

15 L. Wang, W. Song, J. Deng, H. Zheng, J. Liu, Z. Zhao, M. Gao and Y. Wei, *Nanoscale*, 2018, **10**, 6024–6038.

16 P. Chen, Y. Sun, H. Liu, Y. Zhou, G. Jiang, S. C. Lee, Y. Zhang and F. Dong, *Nanoscale*, 2019, **11**, 2366–2373.

17 H. Zhao, X. Liu, Y. Dong, Y. Xia, H. Wang and X. Zhu, *ACS Appl. Mater. Interfaces*, 2020, **12**, 31532–31541.

18 D. Xu, H. Feng, Y. Dong, Q. Wang, G. Zhang, L. Lv, Z. Ren and P. Wang, *Adv. Mater. Interfaces*, 2020, **7**, 2000548.

19 B. X. Li, L. Z. Shao, R. S. Wang, X. P. Dong, F. G. Zhao, P. Gao and Z. Q. Li, *J. Mater. Chem. A*, 2018, **6**, 6344–6355.

20 J. Zhang, S. Chen, L. Qian, X. Tao, L. Yang, H. Wang, Y. Li, E. Zhang, J. Xi, Z. Ji and G. Rohrer, *J. Am. Ceram. Soc.*, 2014, **97**, 4005–4010.

21 R. Li, F. Zhang, D. Wang, J. Yang, M. Li, J. Zhu, X. Zhou, H. Han and C. Li, *Nat. Commun.*, 2013, **4**, 1432.

22 Y. He, J. Li, K. Li, M. Sun, C. Yuan, R. Chen, J. Sheng, G. Leng and F. Dong, *Chin. J. Catal.*, 2020, **41**, 1430–1438.

23 P. Chen, H. Liu, W. Cui, S. C. Lee, L. A. Wang and F. Dong, *EcoMat*, 2020, **2**, e12047.

24 M. Xu, J. Yang, C. Sun, L. Liu, Y. Cui and B. Liang, *Chem. Eng. J.*, 2020, **389**, 124402.

25 Y. Xiao, Z. He, R. Wang, X. Tao and B. Li, *Colloids Surf., A*, 2019, **580**, 123752.

26 L. Wang, D. Cui, L. Ren, J. Zhou, F. Wang, G. Casillas, X. Xu, G. Peleckis, W. Hao, J. Ye, S. X. Dou, D. Jin and Y. Du, *J. Mater. Chem. A*, 2019, **7**, 13629–13634.

27 L. Zhang, Z. Han, W. Wang, X. Li, Y. Su, D. Jiang, X. Lei and S. Sun, *Chem. – Eur. J.*, 2015, **21**, 18089–18094.

28 L. Zhang, W. Wang, S. Sun, D. Jiang and E. Gao, *Appl. Catal., B*, 2015, **162**, 470–474.

29 H. Li, J. Shang, J. Shi, K. Zhao and L. Zhang, *Nanoscale*, 2016, **8**, 1986–1993.

30 Z. Shen, F. Li, J. Lu, Z. Wang, R. Li, X. Zhang, C. Zhang, Y. Wang, Y. Wang, Z. Lv, J. Liu and C. Fan, *J. Colloid Interface Sci.*, 2021, **584**, 174–181.

31 H. Li, Y. Chen, W. Zhou, H. Jiang, H. Liu, X. Chen and T. Guohui, *J. Alloys Compd.*, 2019, **802**, 76–85.

32 X. Yan, X. Zhu, R. Li and W. Chen, *J. Hazard. Mater.*, 2016, **303**, 1–9.

33 X. Zhang, D. An, D. Feng, F. Liang, Z. Chen, W. Liu, Z. Yang and M. Xian, *Appl. Surf. Sci.*, 2019, **476**, 706–715.

34 J. Jiang, K. Zhao, X. Xiao and L. Zhang, *J. Am. Chem. Soc.*, 2012, **134**, 4473–4476.

35 S. Bai, X. Li, Q. Kong, R. Long, C. Wang, J. Jiang and Y. Xiong, *Adv. Mater.*, 2015, **27**, 3444–3452.

36 S. Weng, Z. Pei, Z. Zheng, J. Hu and P. Liu, *ACS Appl. Mater. Interfaces*, 2013, **5**, 12380–12386.

37 Y. Su, L. Zhang, W. Wang and D. Shao, *ACS Sustainable Chem. Eng.*, 2018, **6**, 8704–8710.

38 X. Liu, Z. Chen, J. Shen, M. Ye and W. Chen, *CN 12-1073/TU*, 2010, **16**, 126–129.

39 B. Tian, B. Tian, B. Smith, M. C. Scott, Q. Lei, R. Hua, Y. Tian and Y. Liu, *Proc. Natl. Acad. Sci. U. S. A.*, 2018, **115**, 4345–4350.